

# Analog of Lunar Sun-Synchronous Orbits Based on Spatial Distant Retrograde Orbits

Lei Peng,<sup>\*</sup> Peng Shi,<sup>†</sup> and Yuying Liang<sup>‡</sup>  
*Beihang University, 100191 Beijing, People's Republic of China*

and  
Nishanth Pushparaj<sup>§</sup>  
*University of Nottingham, NG7 2RD Nottingham, United Kingdom*

## I. Introduction

The Moon, the only natural satellite of the Earth, has attracted continuous focus from both the academic and engineering fields, working as the bridge between the near-Earth environment and deep space. Since the first human-crewed lunar mission, the Apollo series [1], more and more lunar exploration missions have been proposed and carried out. These missions aim at the Moon's unique location and in-situ resources, epitomized by NASA's Artemis mission [2], JAXA's SELENE mission in 2007 [3], India's Chandrayaan program [4] and China's series of Chang'e missions [5]. Currently, lunar exploration focuses on long-term residential tasks, i.e., a scientific space station above the Moon [6], which promotes strong needs in long-term orbits around the Moon with very low maintenance costs.

For this purpose, researchers turn to a kind of distant retrograde orbit (DRO) family that shows quite strong stability [7, 8]. Considering the stable motion of the DRO relative to the celestial body, which resembles the motion of a satellite, the DRO is also referred to as a quasi-satellite orbit (QSO) in some literature (e.g., [9-11]), although it is not a true satellite orbit. Originally studied by Hénon [12], the DROs were classified as the family  $f$  when exploring the periodic solution to the Hill's problem in the 1960s. Varying the mass ratio, the DROs' strong stabilities were proved in the circular restricted three-body problem (CR3BP) [7] and elliptic restricted three-body problem [8]. Thus, the cost of orbital maintenance is very low, suggesting that the DROs are ideal destinations for long-term spacecraft [13] or the captured asteroids [14, 15]. In the first phase of NASA's Artemis mission, a DRO was adopted as the transfer target of the uncrewed Orion vehicle for orbital demonstration [2]. Also, by allocating a refueling 'gas station', the lunar DROs can facilitate Earth-Mars transfer and further deep space explorations [16].

---

<sup>\*</sup> Ph.D Candidate, School of Astronautics; lei\_peng@buaa.edu.cn.

<sup>†</sup> Professor, School of Astronautics; shipeng@buaa.edu.cn.

<sup>‡</sup> Professor, School of Astronautics; buaa\_liangyuying@163.com.

<sup>§</sup> Assistant Professor, Nottingham Geospatial Institute; nishanth.pushparaj@nottingham.ac.uk.

Both Peng Shi and Yuying Liang are corresponding authors.

The spatial or three-dimensional DROs (3D DROs) own remarkable advantages in remote sensing, communication, and observation due to their out-of-plane motions in terms of mission operations. Most of the 3D DROs around the Phobos were proved to have high effective stability and low-cost maintenance ( $\sim 1\text{m/s}$  per 9 days) as long-term science orbit for JAXA's MMX mission [11]. Meanwhile, some of the 3D DROs containing moderate escaping/inserting tendencies were employed to construct low-energy transfers connecting the high- and low-altitude science orbits around the Phobos [17]. In the Saturnian system, the highly-inclined 3D DROs around the Enceladus were tested to be stable for 100 days and proved to be the ideal location for long-term observation of polar regions [18].

Besides the stability, the long-term function of spacecraft on the DROs also depends on the sunlight conditions, which have not been properly addressed yet in the aforementioned literature. Frequent switches between shadow and sunlight result in a negative effect on the spacecraft's thermal stability and steady power supply. Therefore, this Note systematically discusses the sunlight issue of the DROs around the Moon, including the distributions of sunlight and the duration of the lunar and Earth shadows in the context of all planar and 3D DRO families, which can be extended to other planetary systems. Furthermore, this Note evaluates the feasibility of the 3D DROs as alternatives to the lunar sun-synchronous orbits (SSOs) through comparisons on the sunlight ratio and shadow duration. Importantly, the dependence of their sunlight conditions is analyzed on the  $z$ -amplitude and resonance in terms of orbital dynamics, providing insights for mission trajectory selection. This analysis can be extended to other celestial bodies with small oblateness (i.e., low  $J_2$  value), whose classic SSOs are limited to a low altitude above the surface.

The Note is organized as follows: **Section II** presents the dynamic model and numerical methods, including continuation, stability, and bifurcation. In **Section III**, the solution map of the Earth-Moon DROs is obtained and the DROs are refined to the perturbed dynamic model. **Section IV** analyzes classic lunar SSOs, proposes the concept of super-sun-synchronous orbit (Super-SSO), and discusses how DROs' sunlight conditions are strengthened by the orbital dynamics. Finally, **Section VI** provides the conclusions.

## II. Background

### A. Dynamic Model

The bi-circular problem (BCP) provides a good approximation of the Sun-Earth-Moon system [19]. As displayed in Fig. 1(a), the BCP comprises a primary body, a subprimary body, a secondary body, and a massless particle, corresponding to the Sun ( $m_S$ ), the Earth ( $m_1$ ), the Moon ( $m_2$ ), and the spacecraft, respectively. In the BCP, the Earth and Moon are assumed to revolve in circular orbits around their barycenter, and the Earth-Moon barycenter is assumed

to move in a circular orbit around the barycenter of the Sun-Earth-Moon system [19]. The orbits of all three bodies are in the same plane. Although this model ignores the Moon's small orbital inclination and eccentricity, which does not satisfy Newton's equations and may introduce minor perturbations, numerical simulations show that it still provides the same qualitative behavior as the real system in certain regions of phase space [19].

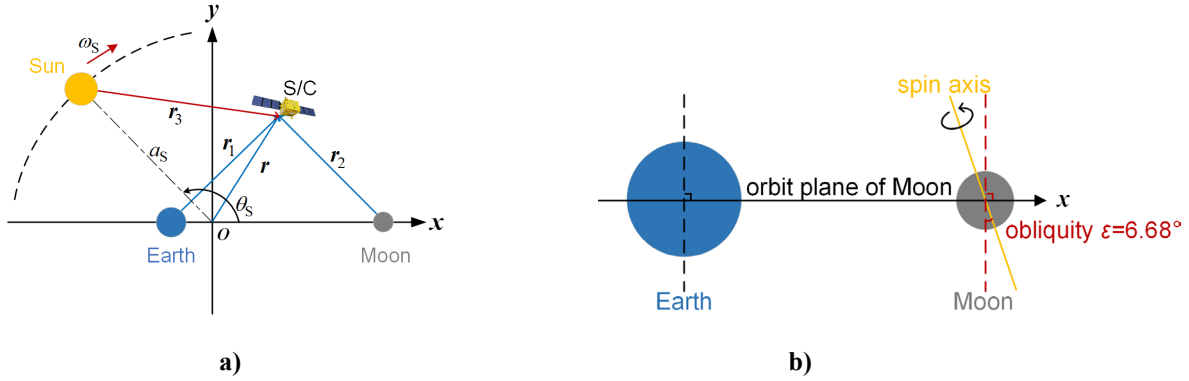


**Fig. 1 The perturbed BCP: a) BCP in the Earth-Moon rotating frame; b) Obliquity of the Moon.**

As shown in Fig. 1(a), a rotating frame ( $O$ - $xyz$ ) is established to describe the motion of the spacecraft: its origin  $O$  coincides with the barycenter of the Earth and the Moon; the  $x$ -axis is directed from the Earth to the Moon; the  $z$ -axis is directed to the angular momentum vector of the Earth-Moon system and the  $y$ -axis obeys the right-hand rule [19]. The unit of mass and length (LU) is taken as the total mass of the Earth-Moon system and the mean Earth-Moon distance, respectively. The period of the Moon moving around the Earth is normalized to  $2\pi$  units of time (TU). Denote  $\mu = m_2/(m_1 + m_2)$  as the mass ratio. Then, the normalized dynamical equations of the spacecraft can be written as [20]

$$\ddot{x} - 2\dot{y} = \frac{\partial \Omega}{\partial x} \quad \dot{y} + 2\dot{x} = \frac{\partial \Omega}{\partial y} \quad \ddot{z} = \frac{\partial \Omega}{\partial z} \quad (1)$$

where  $\Omega$  is the effective potential [21],

$$\Omega = \Omega_{\text{CR3BP}} + \frac{m_s}{r_3} - \frac{m_s}{a_s^2} (x \cos \theta_s + y \sin \theta_s) + \Omega_{\text{Perturb}} \quad (2)$$

$$\Omega_{\text{CR3BP}} = \frac{(x^2 + y^2)}{2} + \frac{(1-\mu)}{r_1} + \frac{\mu}{r_2} + \frac{1}{2} \mu(1-\mu) \quad (3)$$

where  $\Omega_{\text{perturb}}$  indicates the terms affected by the Moon's  $J_2$  and the lunar obliquity in this Note;  $r_1$ ,  $r_2$ , and  $r_3$  denote the distances from the spacecraft to the Earth, the Moon, and the Sun, respectively [20].

$$r_1 = \sqrt{(x+\mu)^2 + y^2 + z^2} \quad r_2 = \sqrt{(x-1+\mu)^2 + y^2 + z^2} \quad r_3 = \sqrt{(x-a_s \cos \theta_s)^2 + (y-a_s \sin \theta_s)^2 + z^2} \quad (4)$$

In particular,  $\theta_s$  satisfies

$$\theta_s = \theta_{s0} + \omega_s t \quad (5)$$

where  $\theta_{s0}$  is the phase angle at the initial epoch  $t_0$  and  $\omega_s$  denotes the normalized angular velocity of the Sun.

According to Muralidharan et al. [22], the perturbing acceleration due to the Moon's  $J_2$  term ( $\sim 10^{-4}$ ) is not negligible for the 4:1 resonant southern  $L_2$  near-rectilinear Halo orbit (NRHO) that has a perilune radius of 4000 km, where  $J_2$ , the second zonal harmonic, is the primary term of the perturbations induced by the Moon's oblateness. Considering that more than 25% of the DROs discussed in this Note have a perilune radius smaller than 5000 km, the perturbation resulting from the Moon's  $J_2$  term cannot be ignored for the DROs. Additionally, both NRHOs and DROs are stable, making the  $J_2$  term crucial for accurately modeling their long-term dynamics. The calculation of the Moon's  $J_2$  term in  $\Omega_{\text{perturb}}$  is relevant to the Moon's obliquity ( $\varepsilon$ ), which indicates the angle between the Moon's orbital and rotational angular velocity vectors [23], as shown in Fig. 1(b).  $\Omega_{\text{perturb}}$  can be expressed as [24]

$$\Omega_{\text{perturb}} = \frac{3A_2}{4}(x_\varepsilon^2 + y_\varepsilon^2) + \frac{\mu A_2}{2r_2^3} \left( 1 - \frac{3z_\varepsilon^2}{r_2^2} \right) \quad (6)$$

$$\begin{bmatrix} x_\varepsilon \\ y_\varepsilon \\ z_\varepsilon \end{bmatrix} = \begin{bmatrix} \cos \varepsilon & 0 & \sin \varepsilon \\ 0 & 1 & 0 \\ -\sin \varepsilon & 0 & \cos \varepsilon \end{bmatrix} \begin{bmatrix} x - (1 - \mu) \\ y \\ z \end{bmatrix} + \begin{bmatrix} 1 - \mu \\ 0 \\ 0 \end{bmatrix} \quad (7)$$

where  $A_2 = (R_E - R_P)/5LU^2$  is the oblateness coefficient of the Moon, representing the second zonal harmonic perturbation in the effective potential term, with  $R_E$  and  $R_P$  denoting the equatorial and polar radius of the Moon, respectively [24, 25].

In this Note,  $\mu = 0.0121506683$ ,  $LU = 384405$  km,  $TU = 4.348113$  days,  $m_s = 328900.541$ ,  $a_s = 388.811143$ ,  $\omega_s = -0.925195985$  rad/s, and  $\varepsilon = 6.68^\circ$  (according to NASA's Moon Fact Sheet) are used in the Sun-Earth-Moon system.

## B. Continuation and Bifurcation of Periodic Orbits

Due to the symmetry about the  $x$ - $z$  plane [12], the initial state of a DRO satisfies that  $y_0 = 0$ ,  $\dot{x}_0 = 0$  and  $\dot{z}_0 = 0$ , i.e.,  $(x_0, 0, z_0, 0, \dot{y}_0, 0)$ . For periodic orbits, the state at half a period is chosen as a reference to check the periodicity because it represents a symmetric phase [12], providing information for the adjustment of the initial state to maintain periodicity through the differential correction method [26]. Therefore, to ensure periodicity, DROs must perpendicularly cross the Poincaré section  $\{\Sigma: y=0\}$  at  $t=T/2$ , where  $T$  denotes the period of the orbit. Mathematically,  $(x_0, z_0, \dot{y}_0)$  should be adjusted such that

$$\mathbf{f}[(x_0, z_0, \dot{y}_0)] = \mathbf{f}(\mathbf{X}_0) = (\dot{x}_{T/2}, \dot{z}_{T/2}) = (0, 0) \quad (8)$$

where the function  $\mathbf{f}(\circ)$  maps the initial state of the DRO orbit to the state at  $t=T/2$  and can be obtained by integrating the dynamical equations (Eq. (1)). Then its Jacobian matrix  $\mathbf{G}=D\mathbf{f}$ .

In this Note, the initial states for DROs are derived from Hénon's  $f$ -family in Hill's problem [12] and are iteratively refined using the aforementioned methods to ensure periodicity within the Earth-Moon CR3BP. Providing that a periodic orbit is computed, it can serve as an initial seed to obtain a whole orbit family through numerical continuation. Among the methodologies available, the pseudo-arclength continuation method, introduced by Keller [26], has been widely adopted in Refs. [9, 11, 27]. By parameterizing the system with an arclength approximation, it can effectively address challenges in path development, especially at limit and bifurcation points.

Given that  $\mathbf{X}_p$  is the  $p$ -th extra solution of the DRO family and its initial guess  $\tilde{\mathbf{X}}_p$ , the initial guess of the next periodic solution is  $\tilde{\mathbf{X}}_{p+1} = \mathbf{X}_p + \Delta s \mathbf{i}_s$ , where  $\Delta s$  is the pseudo-arclength that is manually set as a small parameter (e.g.,  $1 \times 10^{-4}$  in this Note) and  $\mathbf{i}_s$  is the unit vector tangential to the characteristic curve spanned in  $\mathbf{G}$ 's kernel at  $\mathbf{X}_p$  [28]. To correct the error due to linearization, shooting algorithms like differential correction are conducted at  $\tilde{\mathbf{X}}_{p+1}$ , generating the exact solution  $\mathbf{X}_{p+1}$  that corresponds to the next member of the periodic family. The differential correction method iteratively adjusts  $\tilde{\mathbf{X}}_{p+1}$  to minimize the deviation from periodicity, ensuring the orbit maintains its periodic nature [28]. More explicit details of continuation methods can be found in Ref. [28, 29].

In the case that a dynamical system is not structurally stable at some specific parameter values, the system will evolve to a bifurcation point [30]. The bifurcation phenomenon analyzed in this Note is the period-doubling bifurcation, a fundamental mechanism in nonlinear dynamical systems. For CR3BP, the stability information concerning the periodic solution can be indicated from the eigenvalues of its monodromy matrix  $\mathbf{M}$ . It has three pairs of eigenvalues  $\lambda_j$  and  $1/\lambda_j$  ( $j=1, 2, 3$ ), two of which are equal to unity [19]. Given  $\lambda_j = \cos\theta + i\sin\theta$ ,  $1/\lambda_j = \cos\theta - i\sin\theta$ , where  $i$  is the imaginary unit. The corresponding eigenvectors are defined as  $\mathbf{e}_1 \pm i\mathbf{e}_2$  and after one period, they satisfy

$$\mathbf{M}(\mathbf{e}_1 + i\mathbf{e}_2) = [\mathbf{e}_1 \quad \mathbf{e}_2] \begin{bmatrix} \cos\theta & \sin\theta \\ -\sin\theta & \cos\theta \end{bmatrix} = [\mathbf{e}_1 \quad \mathbf{e}_2] \mathbf{R}(\theta) \quad (9)$$

where  $\mathbf{R}(\theta)$  indicates a rotating matrix. To generate a periodic orbit, the cumulative phase difference is  $2k\pi$  (and  $k$  is a positive integer) [11]. Accordingly, the ratio between the number of revolutions around the Moon and  $k$  meets  $n/k = 2\pi/\arccos(v)$ , where  $v = (\lambda + 1/\lambda)/2$  is the stability index of the periodic orbit. Given a pair of  $(n, k)$ , the periodic

solution whose  $\nu$  satisfies the aforementioned relation is a period-doubling bifurcation point corresponding to a resonance of  $n/k$ , and the eigenvectors of  $\lambda$  and  $1/\lambda$  indicate the bifurcation direction [17].

### III. Planar and 3D DRO Families

#### A. Solution Map of DROs via Bifurcation

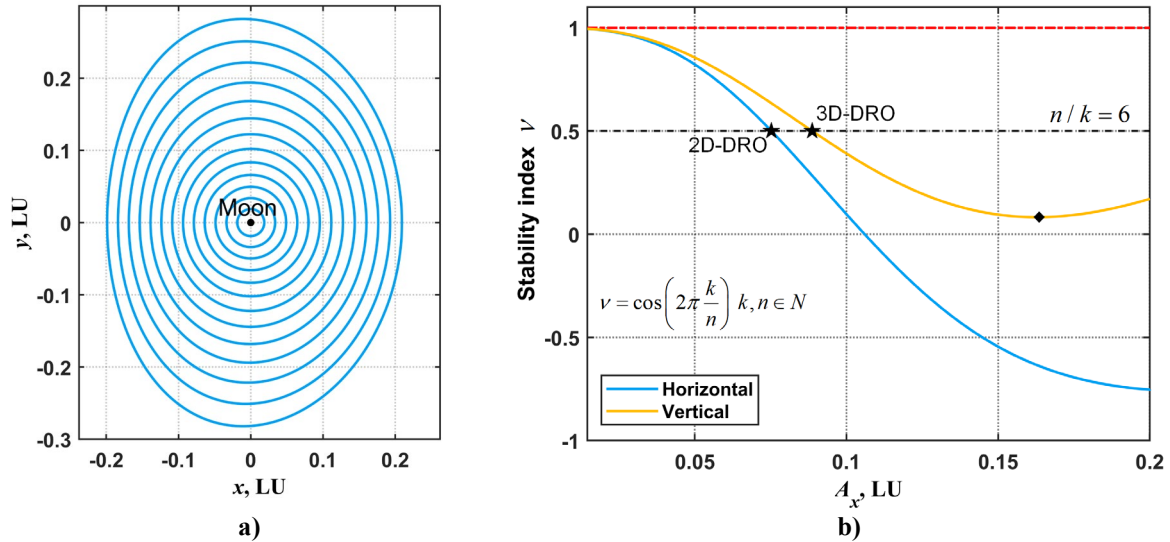


**Fig. 2 Family of planar DROs: a) Orbits in the Moon-centered rotating frame; b) Stability indices.\*\***

This subsection presents the continuation of planar DROs and the bifurcation of 3D DROs in the framework of CR3BP. Figure 2(a) presents the planar DROs generated via the pseudo-arclength continuation method in the Moon-centered rotating frame. The  $x$ -axis amplitude,  $A_x = 1 - \mu - x_0$ , is defined as the initial distance along the  $x$ -direction from the Moon's center to the DRO's initial position, where  $x_0$  indicates the initial  $x$  coordinate of each DRO in the Earth-Moon rotating frame and  $y_0 = 0$ . Figure 2(b) illustrates the horizontal ( $x$ - $y$  plane) and vertical ( $z$ -axis) stability index curve of the planar DRO family. The stability index, denoted as  $\nu$ , is calculated as  $\nu = (\lambda + 1/\lambda)/2$ , where  $\lambda$  is the eigenvalue of monodromy matrix  $\mathbf{M}$  corresponding to the horizontal (vertical) direction. The vertical stability index is derived from the vertical eigenvalue, whose eigenvector has an out-of-plane ( $z$ -direction) component. When  $|\nu| > 1$ , the orbit is considered unstable, whereas for  $|\nu| \leq 1$ , the orbit is stable. As discussed in **Section II.B**, the stability index allows for the identification of bifurcation points for periodic DROs, with the bifurcation condition given by  $n/k = 2\pi/\arccos(\nu)$ . As an example, the black stars in Fig. 2(b) indicate in-plane and out-of-plane 6-period-doubling bifurcation points ( $\nu = 0.5$ ). The 3D DROs are bifurcated from the vertical stability index curve while the planar DROs

\*\* The necessary data for the figures presented in the Note are available in the supplementary material.

are bifurcated from the horizontal one. The black diamond indicates the minimum value of  $n/k$ , which is 4.22, thus the minimum number of revolutions  $n$  is 5 regarding the bifurcation of 3D DROs (see last section).

To provide a comprehensive analysis of 3D DROs and their characteristics such as stability, sunlight conditions, and so on, we systematically derive the family of 3D DROs. Leveraging the period-doubling bifurcation methods discussed in **Section II.B**, the first spatial DRO for each resonance is computed by applying the differential correction algorithm to the initial guess derived from the bifurcation point of the planar DRO family. These orbits are then extended using the pseudo-arclength continuation method, generating other members of the 3D DRO family. Figure 3 shows the bifurcated families searched with  $k=1$  and  $n>5$ . The tint of color indicates the stability index of each orbit. The horizontal axis indicates  $A_x$ , and the vertical axis indicates  $A_z=z_0$ . In a similar manner to Chen et al. [11], the  $y$ -amplitude ( $A_y$ ) is defined as the maximum value of the orbit on the  $+y$  axis, which is not shown in the solution map for simplicity. The pink line at  $A_z=0$  indicates the planar family of DROs (blue lines in Fig. 2(a)), from which all of the bifurcated families are generated. In particular, at each resonance ( $n/k$ ), a primary branch is produced from the vertical stability index curve and extends towards high  $A_z$  via continuation, while during its continuation, a secondary branch is then generated. For the primary branch, as  $n/k$  increases, the average value of  $A_x$  gradually decreases, i.e., DROs with larger resonances are closer to the Moon.

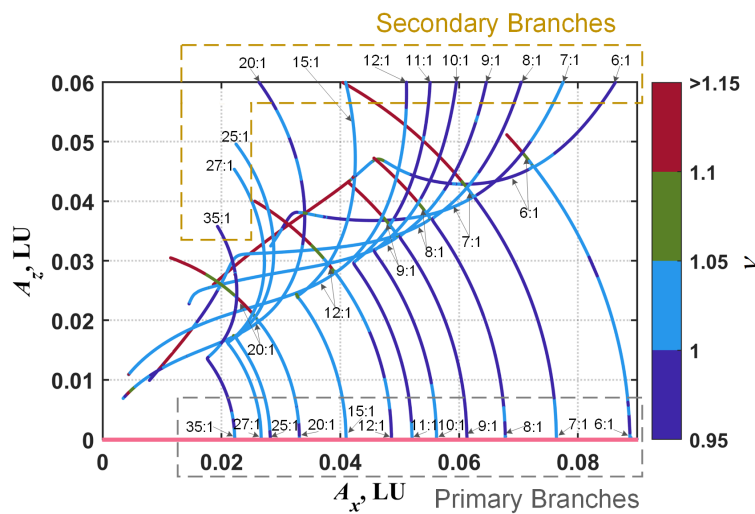


**Fig. 3 Solution map of bifurcated DRO families.**

Figure 4 illustrates four sample DROs with  $n/k=9:1$  (subplot (a) and (b)) and  $20:1$  (subplot (c) and (d)) of the primary branch (left panel) and the secondary branch (right panel) in the Moon-centered rotating frame. The DRO of the primary branch is symmetric about the  $x$ - $y$  plane, while the secondary branch is asymmetric. As shown by their

projections to the  $x$ - $y$  plane, the DROs of the secondary branch (subplot (b) and (d)) generally expand in a larger scale than the primary one geometrically, giving more opportunities in shadow avoidance.

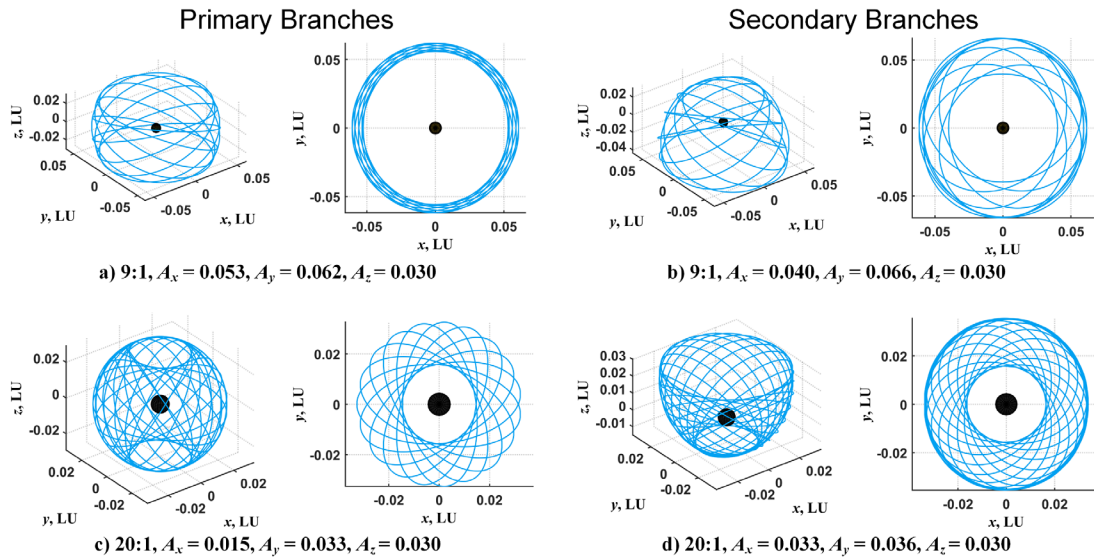


Fig. 4. DROs from different families at  $A_z=0.030$ .

### B. Refinement of DROs under Multiple-Perturbations

A quick calculation of our DROs shows that the Moon's  $J_2$  is about ten times larger than the Earth's  $J_2$ . Thus, the DROs produced in the CR3BP of the last subsection are refined to the BCP under the Moon's  $J_2$  perturbation and lunar obliquity. A multiple shooting algorithm is introduced to deal with the refinement [31]. Mathematically, the algorithm iteratively optimizes the state vector at each patched point to obtain an optimal solution satisfying the continuity constraints between subintervals under a certain tolerance. For the detailed solution procedure, see Ref. [31]. Figure 5 presents a refined trajectory of 9:1 3D DRO (Fig. 4(a)) in three years.

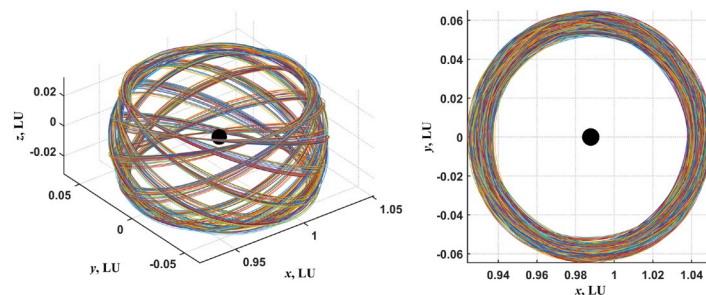


Fig. 5. An example of corrected quasi-periodic DRO for three years.

## IV. Super-Sun-Synchronous Orbit

In this section, comparisons on the orbital characteristics and sunlight conditions are conducted between the classic lunar SSOs and the DROs around the Moon. Based on the requirement of the Chang'e-4 mission, a concept of super-

sun-synchronous orbits (Super-SSOs) is proposed among DROs as promising alternatives to the classic SSOs. Furthermore, particular attention is given to lunar and Earth's shadows and their dependence on the  $z$ -amplitude ( $A_z$ ) and resonance ( $n/k$ ). Besides, the way to search the full-domain sunlight orbit is provided.

### A. Comparisons to Sun-Synchronous Orbits

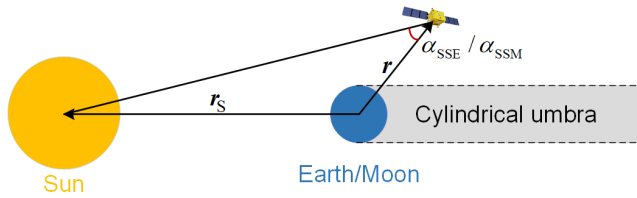


**Fig. 6. Cylindrical shadow model.**

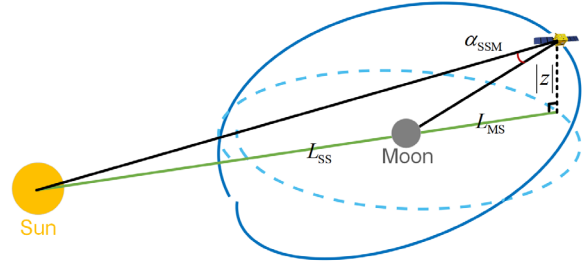


**Fig. 7.  $\alpha_{SSM}$  of the 'collinear point'.**

The cylindrical shadow model (see Fig. 6) is adopted to approximate the sunlight of a spacecraft around the Moon. According to the results of Hubaux et al. [32], angles  $\alpha$  and  $\beta$  represent the geometric difference between the cylindrical and conical shadow models (see Fig. 4 of Ref. [32]). The penumbra region bounded by  $(\alpha+\beta)$  is only about 0.26 degrees, indicating that the cylindrical model is an accurate approximation. A smooth shadow function is introduced to model the shadow crossing, which is defined as [32]

$$v_c(\mathbf{r}) = \frac{1}{2} \left\{ 1 + \tanh \left[ \gamma \left( \frac{\mathbf{r} \cdot \mathbf{r}_s}{r_s} + \sqrt{r^2 - R^2} \right) \right] \right\} = \begin{cases} 0 & \text{in cylindrical umbra} \\ 1 & \text{otherwise} \end{cases} \quad (10)$$

where  $\gamma$  is a parameter controlling the sharpness of  $v_c(\mathbf{r})$  and set to  $1 \times 10^9$  to mimic a cylindrical umbra [32],  $\mathbf{r}$  and  $\mathbf{r}_s$  are shown in Fig. 6, and  $R$  represents the equatorial radius of the planet.

In this Note, the Sun-Spacecraft-Moon (SSM) angle  $\alpha_{SSM}$  and the Sun-Spacecraft-Earth (SSE) angle  $\alpha_{SSE}$  (see Fig. 6) are presented to show the distribution of the lunar and Earth's shadow, respectively. The shadow appears when  $\alpha_{SSM}$  or  $\alpha_{SSE}$  is below a certain threshold, which is determined by the size of the occulting body [33] and the distance from the spacecraft to the occulting body. Figure 7 shows that the minimum  $\alpha_{SSM}$  in a single revolution of the DRO appears near the 'collinear point', where the spacecraft's projection in the  $x$ - $y$  plane is collinear with the Sun and Moon.

The generation of an SSO involves utilizing the secular variation of the ascending node angle induced by the celestial body's oblateness (consider the  $J_2$  term), allowing the orbit plane to remain aligned with the Sun-line throughout the year without the need for propellant [34]. Hence, the standard SSO can be found as [34]

$$i_{\text{SSO}} = \arccos \left( -\frac{\Delta\Omega a^{3.5} (1-e^2)^2}{1.5J_2 \sqrt{\mu_M} R_M^2} \right) \quad (11)$$

where  $\mu_M$  is the lunar gravitational constant,  $\Delta\Omega$  is the mean rotation rate of the Sun in the inertial reference frame per second, and  $R_M$  is the Moon's radius. Figure 8 illustrates the distribution of orbital elements ( $a$ ,  $e$ ,  $i_{\text{SSO}}$ ) of the lunar SSOs, all of which are retrograde around the Moon because their values of  $i_{\text{SSO}}$  exceed 90 degrees, a characteristic also exhibited by DROs. The number of lunar SSOs is extremely limited due to the small lunar  $J_2$  term. Note that the value of  $i_{\text{SSO}}$  becomes smaller as the acute orbital angle (referred to as the orbital inclination in the following texts) with respect to the lunar equator goes higher. The theoretical minimum  $a$  of the lunar SSOs is achieved at  $R_M$  (1737.1 km), which leads to the highest inclination (the smallest value of  $i_{\text{SSO}}$ , blue star in Fig. 8). As demonstrated in Fig. 8, the higher orbital inclination results in the lower orbital altitude above the Moon's surface. According to Liang and Hyodo [23], the shadow duration is increased as the orbital altitude or the orbital inclination decreases. This indicates a trade-off in classic SSOs: while increasing orbital inclination can shorten shadow duration, it simultaneously decreases orbital altitude, which extends the shadow duration. This inherent conflict limits their ability to achieve favorable sunlight conditions. Consequently, the SSOs are unsuitable for lunar spacecraft that are sensitive to frequent switches of sunlight and shadow or that request full-domain sunlight.

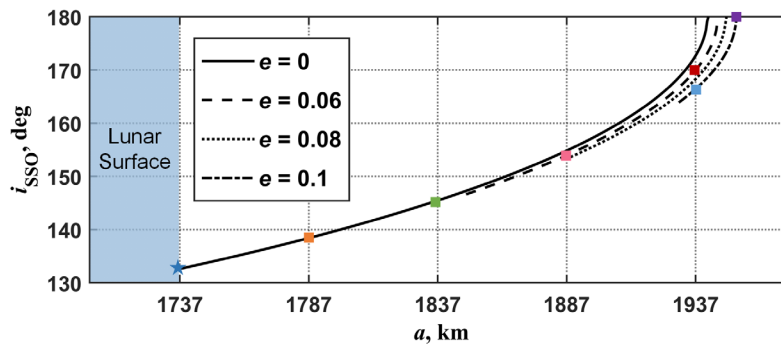


**Fig. 8. Orbital elements of the lunar SSOs.**

To quantify the sunlight conditions, we introduce two indices:  $\eta_S$  denotes the ratio of sunlight duration in a lunar spacecraft's lifetime cycle;  $d_S$  denotes the longest shadow duration. In this Note, we set the spacecraft's lifetime as three years, following the Chang'e-4 mission, which allocated a relay spacecraft around  $L_2$  point for about three years [35]. The sunlight ratio ( $\eta_S$ ) determines the cumulative impact of sunlight and the sunlight supply of the mission. The shadow duration ( $d_S$ ) is related to the design of the spacecraft's power system, e.g., the battery capacity.

**Table 1 Sunlight indices of the SSOs around the Moon**

Color marker	$e$	$a$ , km	$\eta_s$	$d_s$ , minute
Orange	0	1787	57.36%	585.61
Green	0	1837	60.46%	984.89
Pink	0.06	1887	61.99%	787.91
Red	0.06	1937	64.08%	591.37
Blue	0.10	1937	63.40%	591.37
Purple	0.10	1952	63.90%	591.37

Table 1 presents the value of  $\eta_s$  and  $d_s$  of the lunar SSOs with an eccentricity of 0, 0.06, and 0.1, with all the points marked by squares in Fig. 8. It suggests that almost half of the lifetime cycle is shadowed by the Moon and Earth meanwhile the lunar spacecraft will suffer from no solar power longer than 9 hours. Therefore, it is of engineering significance to develop a new orbit around the Moon with better sunlight (i.e., larger  $\eta_s$  and shorter  $d_s$ ) to replace the current lunar SSOs to solve the power issue.

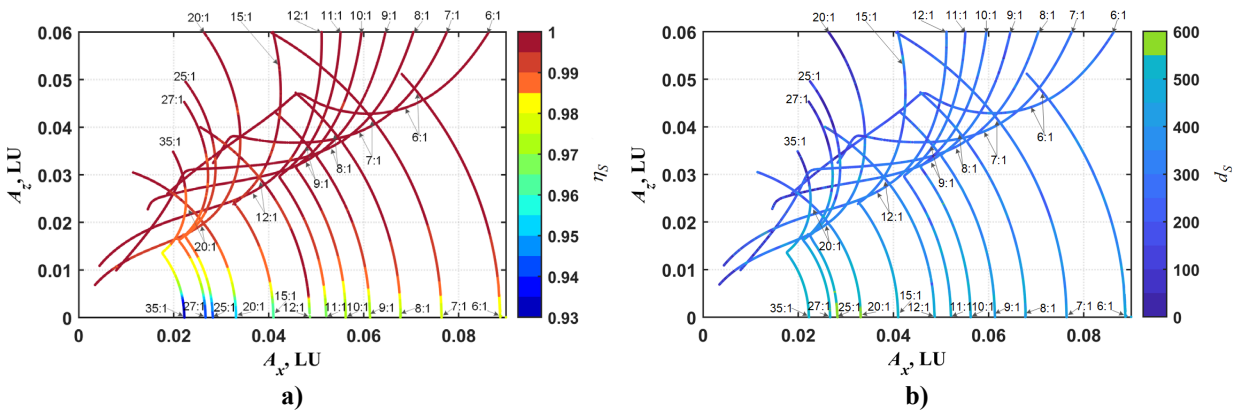


**Fig. 9. Sunlight indices maps of all the DROs with  $\theta_{s0}=0$ : a) Sunlight ratio; b) The longest shadow duration.**

Figure 9 illustrates the sunlight indices  $\eta_s$  (subplot (a)) and  $d_s$  (subplot (b)) for all the DROs where the tint of color indicates their values. It suggests that all of the DROs have superior sunlight over the lunar SSOs (see Table 1 as a comparison) and thereby as the replacement of the classic SSOs. Thus, combining the engineering requirements with the performances of the SSOs, we propose a new concept of super-sun-synchronous orbits (Super-SSOs). Super-SSOs are defined as DROs that have a sunlight ratio larger than 98.5% (according to the working status of the relay satellite of the Chang'e-4 mission [35]) and the maximum shadow duration shorter than 550 minutes (less than the minimum  $d_s$  of lunar SSOs). Furthermore, except for a few DROs with very small  $A_z$ , most of them can be defined as Super-SSOs. Note that the number of Super-SSOs is much greater than that of classic lunar SSOs, providing a much wider range of orbit selections. Additionally, while lunar SSOs maintain a fixed angle between the orbital plane normal and the Sun-Moon vector, allowing stable orientation of the spacecraft without continuous adjustments, Super-SSOs can also achieve similar functionality. Our result shows that by employing a simple PD controller, the solar arrays can be

efficiently adjusted to follow the sunlight direction with little control cost and energy consumption, further demonstrating their suitability as practical alternatives to lunar SSOs.

Furthermore, Super-SSOs are not only limited to the Moon and can be applied to other systems with low oblateness, such as small moons (e.g., Phobos or Deimos) and dwarf planets (e.g., Ceres). For these celestial bodies, where classic SSOs are constrained to low altitudes and offer very few viable orbits due to small  $J_2$  term, Super-SSOs can provide improved sunlight conditions. These features are particularly beneficial for spacecraft requiring continuous or extended sunlight exposure, making Super-SSOs a practical solution for orbit design in diverse dynamic systems.

## B. Lunar shadow

In this Note, a spacecraft on the Super-SSO around the Moon is shadowed by the Moon and the Earth. This subsection discusses how the lunar shadow of the Super-SSOs is influenced by the  $z$ -amplitude ( $A_z$ ) and the bifurcation resonance ( $n/k$ ).

### 1. Dependence on $z$ -amplitude

As an example, we focus on the Super-SSOs on the primary branch with  $n/k$  of 7:1, considering  $A_z$  values of 0.01 LU, 0.02 and 0.04 LU. Figure 10 presents the evolution of  $\alpha_{SSM}$ . Green lines indicate its evolution, and blue marks indicate the epoch when the lunar shadow appears.

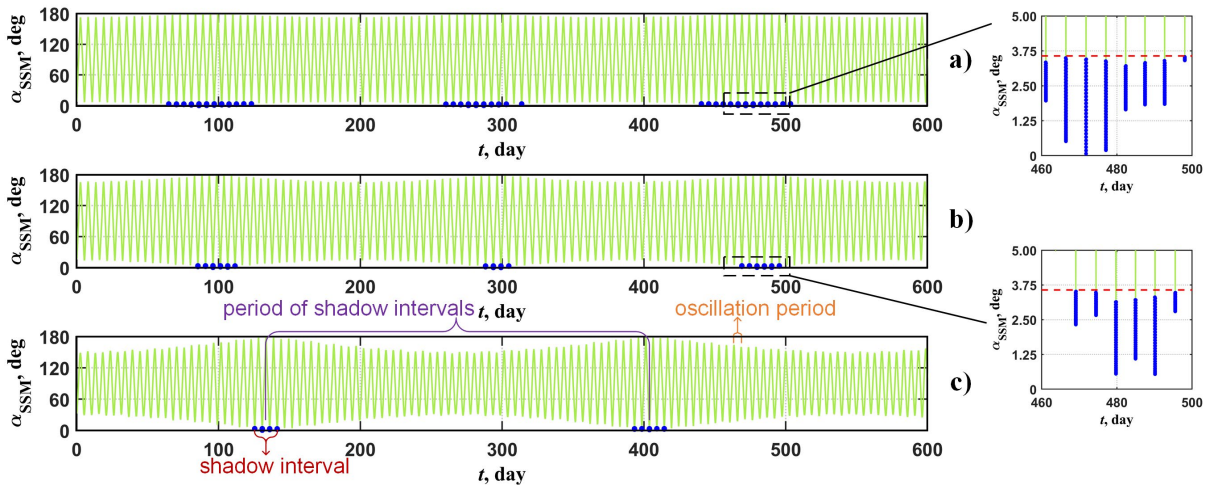


**Fig. 10.** Evolution of  $\alpha_{SSM}$  for 7:1 Super-SSOs with different  $A_z$ : a)  $A_z=0.01$  LU; b)  $A_z=0.02$  LU; c)  $A_z=0.04$  LU.

The lunar shadow occurs when  $\alpha_{SSM}$  falls below a certain threshold, as indicated by the blue marks in Fig. 10. The value of this threshold is influenced by both the size of the occulting body [33] and the distance between the spacecraft and the occulting body at the given epoch. Consequently, for Super-SSOs with the same resonance, variations in  $A_z$

do not significantly impact the spacecraft-Moon distance, leading to little variation in the threshold of lunar shadow. For instance, for the 7:1 Super-SSOs, the threshold is approximately 3.57 degrees, as exhibited by the red dashed lines in the magnified views of Fig. 10. Furthermore, due to the fact that the Sun is in retrograde circular motion around the Earth-Moon system in our problem, the oscillation period (5.26 days) of  $\alpha_{SSM}$  is longer than the single revolution of this 7:1 Super-SSO around the Moon (4.52 days). The minimum  $\alpha_{SSM}$  (at the ‘collinear point’) is  $\alpha_{SSM,\min} = \arctan(L_{SS}/|z|) - \arctan(L_{MS}/|z|)$ , where  $L_{SS}$  and  $L_{MS}$  represent the distances from the projection point on the  $x$ - $y$  plane to the Sun and the Moon, respectively (see Fig. 7).  $|z|$  denotes the modulus of the  $z$ -component. Since  $|z|$  will not exceed  $\sqrt{L_{SS}L_{MS}}$ , for Super-SSOs belonging to the same resonance family,  $\alpha_{SSM,\min}$  increases with the growing  $|z|$  corresponding to the ‘collinear point’, as shown in the magnified views of Figs. 10(a) and 10(b), where  $\alpha_{SSM,\min}$  of the Super-SSO with higher  $A_z$  (Fig. 10(b)) is larger. It suggests that spacecraft on the Super-SSOs with higher  $A_z$  are more likely to escape the lunar shadows, which agrees with the results of Liang and Hyodo [23].

As shown by the blue marks in each subplot of Fig. 10, the distributions of lunar shadows appear in a certain period (about 180 days in subplot(a), 200 days in subplot(b), and 270 days in subplot(c)). The time interval of sequential distributions of lunar shadows is referred to as a shadow interval in the following texts and the interval between two sequential distributions is denoted as the period of shadow intervals. As  $A_z$  increases, the length of the shadow interval is shortened because of the increased  $z$ -direction velocity  $V_z$ . As shown by the black solid, dashed and dotted lines of Fig. 11, a Super-SSO with larger  $A_z$  has larger  $V_z$  and it crosses the cylindrical shadow faster, leading to a smaller length of the shadow interval with a longer period.

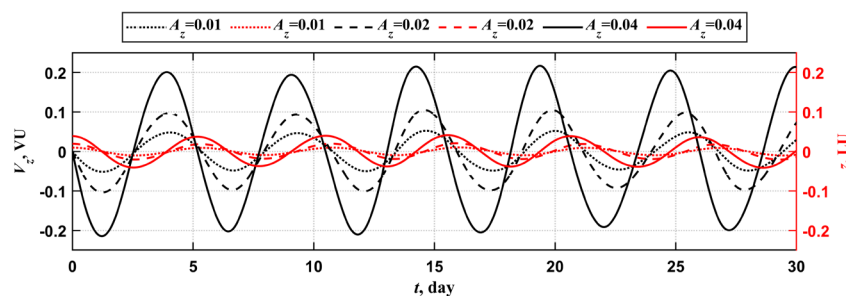


**Fig. 11. Evolution of  $z$ -direction component and velocity for the 7:1 Super-SSOs with different  $A_z$ .**

In conclusion, to effectively avoid lunar shadows, it is suggested to select a Super-SSO with a larger  $A_z$  that has a longer period and smaller length of shadow intervals. Furthermore, due to the fact that the lunar shadow intensively occurs, a spacecraft with strict sunlight requests is able to continuously function outside the lunar shadow intervals for more than 180 days.

## 2. Dependence on the resonance

Besides the  $z$ -amplitude, the sunlight of Super-SSOs also depends on the resonance ( $n/k$ ). To explore its effect, we take the Super-SSOs from the primary branches with  $n/k$  values of 6, 9, and 12, with the same  $A_z$  (0.02 LU). Figure 12 presents the three-year evolution of  $\alpha_{SSM}$  for these orbits.

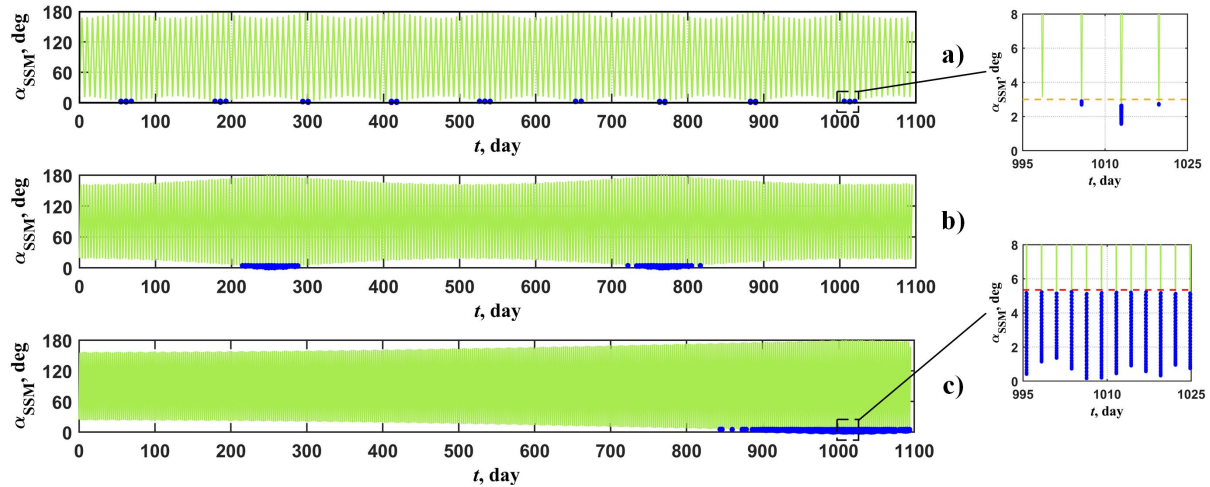


**Fig. 12. Evolution of  $\alpha_{SSM}$  for the Super-SSOs with different resonances: a)  $n/k=6$ ; b)  $n/k=9$ ; c)  $n/k=12$ .**

As illustrated in the magnified views of Figs. 12(a) and 12(c), Super-SSOs with higher resonances exhibit faster variations of  $\alpha_{SSM}$  (e.g., for  $n/k=6$ , the period is about 7.50 days, while for  $n/k=12$ , it is about 2.73 days), which is due to the denser orbital configuration of Super-SSOs with higher resonances. Moreover, the threshold of  $\alpha_{SSM}$  corresponding to the lunar shadow increases significantly with the resonance. This trend is evidenced by the orange dashed line in the magnified view of Fig. 12(a) (about 3.00 degrees) and the red dashed line in Fig. 12(c) (about 5.35 degrees). Essentially, the increase in the threshold is attributed to the reduction in the average distance between the Super-SSO and the Moon as the resonance increases, as observed in the comparison between Figs. 4(a) and 4(c).

Similar to the results of  $z$ -amplitude, as the resonance increases, the period of the shadow interval is enlarged (about 110 days in subplot(a), 520 days in subplot(b), and 1800 days in subplot(c)) but its length becomes larger (about 20 days in subplot(a), 80 days in subplot(b), and 300 days in subplot(c)). The tendency can also be explained by the dynamics of the Super-SSOs. As shown by the black solid, dashed, and dotted lines of Fig. 13, a Super-SSO with a larger resonance has a larger  $V_z$ . Thus, it is easier to escape from the lunar shadow, leading to a longer period of the shadow interval, which is similar to the results of  $z$ -amplitude. However, with different resonances, the oscillation period of the Super-SSOs varies. It takes more revolutions of the Super-SSOs to pass the cylindrical lunar shadow, resulting in a larger length of the shadow interval.

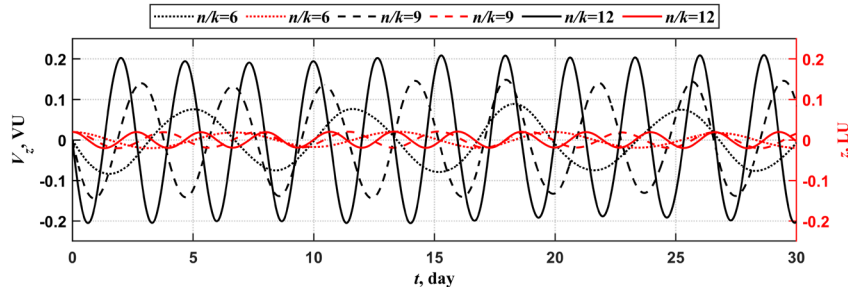


**Fig. 13. Evolution of  $z$ -direction component and velocity for the Super-SSOs with different resonances.**

Thus, one must be very careful when choosing Super-SSOs with large resonances. For a large resonance (e.g., 12), a spacecraft on the Super-SSO can completely stay free from lunar shadow for over 2.5 years. Nevertheless, if the spacecraft is inserted into this Super-SSO at the beginning of the shadow interval, it is trapped in the frequent switches of sunlight and shadow every 2.5 days over one year, posing significant challenges for the thermal system.

### C. Earth's Shadow

This subsection presents the distribution of the Earth's shadow dependent on the  $z$ -amplitude and the resonance (Fig. 14). Blue lines indicate the evolution of  $\alpha_{SSE}$ , and the black marks indicate the occurrence of the Earth's shadow.

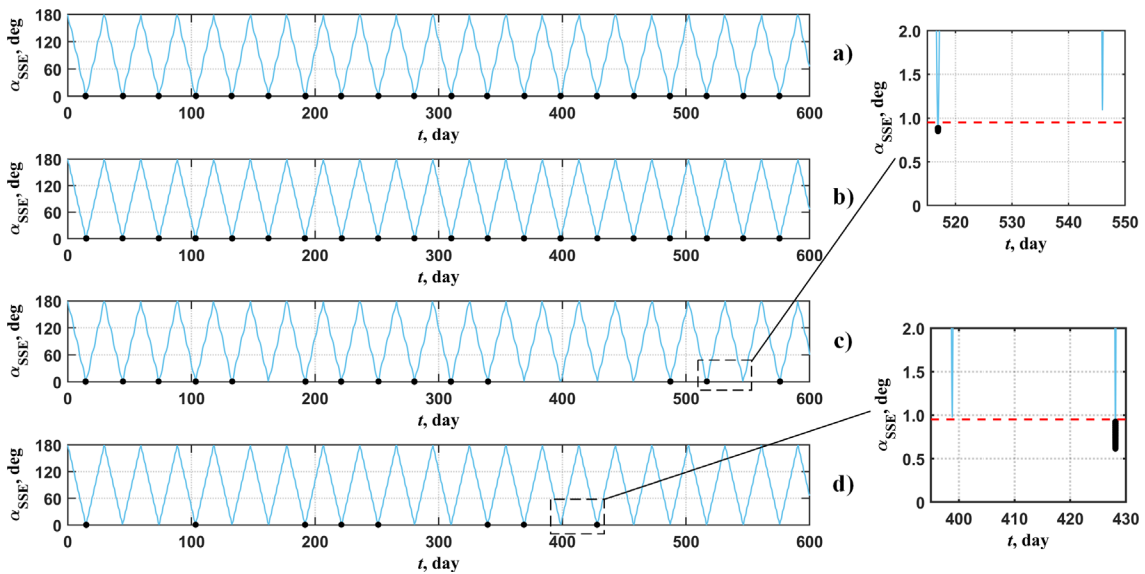


**Fig. 14. Evolution of  $\alpha_{SSE}$  for the Super-SSOs: a)  $n/k=7$ ,  $A_z=0.01$  LU; b)  $n/k=15$ ,  $A_z=0.01$  LU; c)  $n/k=7$ ,  $A_z=0.02$  LU; d)  $n/k=15$ ,  $A_z=0.02$  LU.**

Due to the fact that the phase angle of the spacecraft with respect to the Earth does not change as dramatically as that to the Moon ( $0-2\pi$ ), the oscillation period of  $\alpha_{SSE}$  approximately equals to the Sun's synodic period (29.53 days) for all Super-SSOs. Different from the results of the lunar shadow (Fig. 10), there does not exist intensively distributed shadow by the Earth, but it could occur every oscillation period of  $\alpha_{SSE}$ . The Earth's shadow is observed when  $\alpha_{SSE}$

drops below a specific threshold (about 0.95 degrees, red dashed line in Fig. 14), indicating alignment between the spacecraft, Earth, and Sun. Points not marked in Fig. 14 correspond to states where  $\alpha_{SSE}$  does not meet this condition, as illustrated in the magnified views of Fig. 14(c) and (d). Increasing  $z$ -amplitude or resonance can prevent the Earth's shadow at certain oscillation periods. This is due to higher  $z$ -direction velocity ( $V_z$ ), which enables quicker escape from the shadow (subplots of Fig. 14), as explained for the lunar shadow in **Section IV.B**. Thus, with the introduction of Earth, conclusions related to the lunar shadow are not profoundly altered. For example, as confirmed in Fig. 15, a spacecraft on the Super-SSO ( $n/k=9$ ,  $A_z=0.037$  LU,  $\theta_{S0}=5\pi/3$ ) can completely prevent mutual shadow for over 1.5 years.

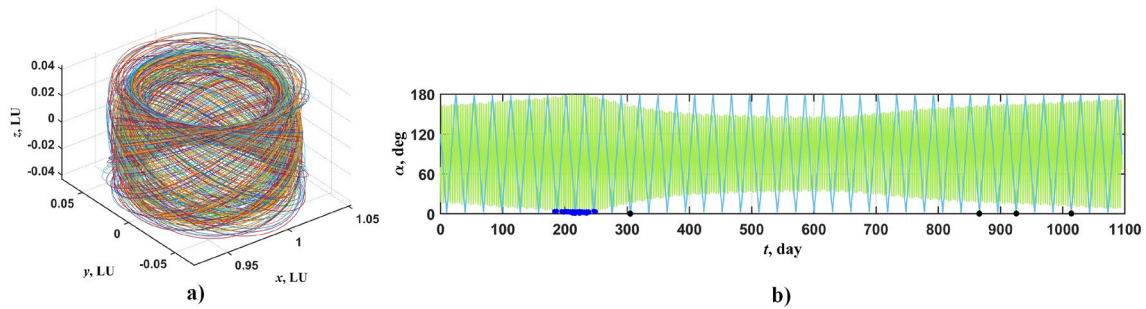


**Fig. 15. An example of the Super-SSO with sunlight over 1.5 years: a) The Super-SSO; b) The blue line indicates the evolution of  $\alpha_{SSE}$  and the green line indicates the evolution of  $\alpha_{SSM}$ .**

#### D. Super-SSOs with Full-Domain Sunlight

In the previous subsections, it is concluded that the Super-SSOs are a better replacement for classic SSOs regarding the sunlight ratio ( $\eta_s$ ) and shadow duration ( $d_s$ ). Furtherly, among the Super-SSOs, those with higher  $z$ -amplitude and resonance can prevent both lunar and Earth's shadows for over 1.5 years. Nevertheless, it still remains an open question whether there exists a Super-SSO with full-domain sunlight for three years or longer.

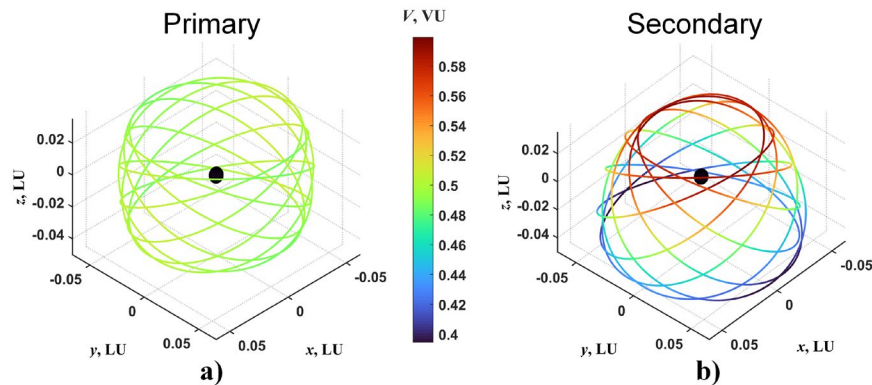


**Fig. 16. Velocity of the Super-SSOs in different branches: a) Primary branch; b) Secondary branch.**

Figure 16 shows the velocity distribution of two Super-SSOs from primary and secondary branches with the same resonance and  $z$ -amplitude ( $n/k=9$ ,  $A_z=0.03$  LU). According to our conclusions in **Section IV.B**, the spacecraft is more

likely to be shadowed when it is closer to the Moon, and the shadow duration is associated with the arc length of the trajectories intersected by the cylindrical shadows. Thus, the full-domain sunlight may appear if the spacecraft moves faster when closer to the Moon's surface, preventing it from being shadowed, thereby suggesting both its trajectory and velocity are distributed nonuniformly. However, as presented in Fig. 16(a), the velocity distribution of the Super-SSO in the primary branch is almost uniform and symmetrical about the  $x$ - $y$  plane. Thus, it is difficult for its trajectory to stay outside both the Earth and the lunar cylindrical shadows to achieve full-domain sunlight, as is also confirmed by our numerical results. Nevertheless, due to the asymmetric shape of the Super-SSOs in the secondary branches (subplot (b)), the spacecraft moves faster as it is closer to the Moon's surface and its velocity greatly decreases (from 0.59 VU to 0.40 VU,  $VU=LU/TU$ ) as it moves outwards from the Moon. Thus, the sunlight conditions can be significantly improved for the Super-SSO members from the secondary branches (subplot (b) and (d) in Fig. 4).

As an example, a Super-SSO with full-domain sunlight is searched with  $n/k=20$ ,  $A_z=0.04$  LU,  $\theta_{S0}=\pi$  (subplot (a) of Fig. 17), and during the tested period of time (three years), the spacecraft on this Super-SSO is supposed to escape the Earth and the Moon shadows completely (see subplot (b) of Fig. 17).

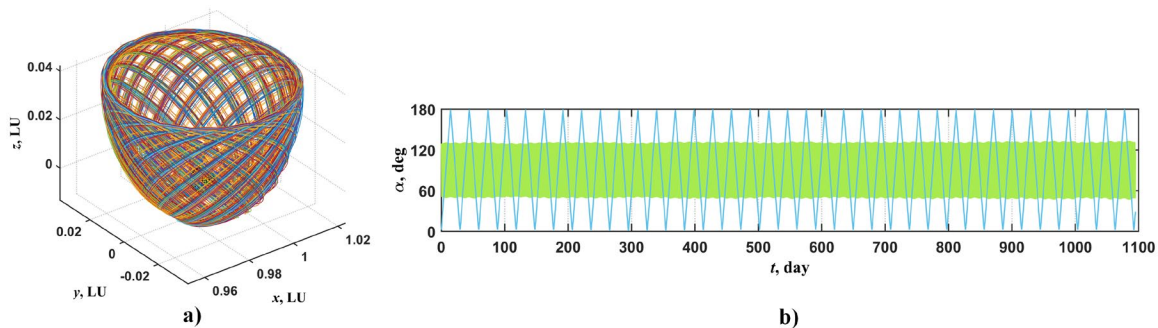


**Fig. 17. An example of the Super-SSO in a secondary branch with full-domain sunlight: a) the Super-SSO; b) the blue line indicates the evolution of  $\alpha_{SSE}$  and the green line indicates the evolution of  $\alpha_{SSM}$ .**

## V. Conclusion

This Note is devoted to providing orbits for long-term lunar exploration missions requiring favorable sunlight. Initially, the classic lunar SSOs are found not to have good sunlight as expected due to the small lunar oblateness. To address the issue, the DROs with long-term stability are considered. Along the planar DROs, the 3D DRO families with certain resonances are obtained by continuation and bifurcation methods, accounting for perturbations such as solar gravity, lunar  $J_2$ , and obliquity. It is found that all the DROs work better than the lunar SSOs regarding the sunlight conditions, demonstrating that they are promising alternatives to the lunar SSOs. Most 3D DROs are unshadowed for over 98.5% of three years with the longest shadow shorter than 550 minutes, referred to as Super-

SSOs in this Note. Notably, these Super-SSOs can also be applied to celestial bodies with small oblateness, where classic SSOs exhibit poor sunlight conditions.

Moreover, the lunar and Earth's shadows exhibit sensitivity to the Super-SSOs' dynamic characteristics ( $z$ -amplitude and resonance). For the lunar shadows, higher  $z$ -amplitude enhances sunlight conditions, while increasing resonance extends both the shadow interval's period and length. Increasing  $z$ -amplitude or resonance prevents Earth's shadows at some oscillation periods, not significantly altering conclusions regarding lunar shadows. Furthermore, efforts are devoted to obtaining full-domain sunlight orbits. Analyzing the dynamic properties of 3D DROs, i.e., the velocity distribution, demonstrates that the Super-SSOs with full-domain sunlight are more likely to exist in the secondary branches. Further investigation identifies a Super-SSO completely free of shadows over three years.

In conclusion, the superior sunlight conditions of the Super-SSOs make them completely capable of replacing classic lunar SSOs, thereby facilitating the realization of long-term and sustainable lunar missions.

### Acknowledgments

Y. Liang acknowledges the support of the National Natural Science Foundation of China (12302053) and Shanghai Academy of Spaceflight Technology (SAST2023-045). S. Peng acknowledges the support of the Joint Funds of the National Natural Science Foundation of China (U23B6002). N. Pushparaj acknowledges the support of the University of Nottingham through the Early Career Fund and International Research Collaboration Fund.

### References

- [1] Johnston, R. S., and Hull, W. E., *Apollo Missions*, Biomedical Results of Apollo, eds RS Johnston, LF Dietlein and C. Berry (Washington, DC: National Aeronautics and Space Administration), 1975, pp. 9-40.
- [2] Batcha A. L., Williams J., Dawn T. F., Gutkowski J. P., Widner M. V., Smallwood S. L., Killeen B. J., Williams E. C., and Harpold R. E., "Artemis I Trajectory Design and Optimization," *2020 AAS/AIAA Astrodynamics Specialist Conference*, No. AAS 20-649. 2020.
- [3] Matsunaga, T., Ohtake, M., Hirahara, Y., and Haruyama, J., "Development of A Visible and Near-Infrared Spectrometer for Selenological and Engineering Explorer (SELENE)," *Hyperspectral Remote Sensing of the Land and Atmosphere*, SPIE, Vol. 4151, 2001, pp. 32-39.  
<https://doi.org/10.1117/12.417021>

- [4] Durga Prasad, K., Bhatt, M., Ambily, G., Sathyan, S., Misra, D., Srivastava, N., and Bhardwaj, A., "Contextual Characterization Study of Chandrayaan-3 Primary Landing Site," *Monthly Notices of the Royal Astronomical Society: Letters*, Vol. 526, No. 1, 2023, pp. L116-L123.  
<https://doi.org/10.1093/mnrasl/slad106>
- [5] Xiao, L., Qian, Y., Wang, Q., and Wang, Q., *The Chang 'E-5 Mission*, Sample return missions. Elsevier, 2021, pp. 195-206.  
<https://doi.org/10.1016/B978-0-12-818330-4.00009-4>
- [6] Pittman, R. B., Harper, L. D., Newfield, M. E., and Rasky, D. J., "Lunar Station: The Next Logical Step in Space Development," *New Space*, Vol. 4, No. 1, 2016, pp. 7-14.  
<https://doi.org/10.1089/space.2015.0031>
- [7] Benest, D., "Effects of the Mass Ratio on the Existence of Retrograde Satellites in the Circular Plane Restricted Problem," *Astronomy and Astrophysics*, Vol. 32, 1974, pp. 39.
- [8] Broucke, R., "Stability of Periodic Orbits in the Elliptic, Restricted Three-body Problem," *AIAA journal*, Vol. 7, No. 6, 1969, pp. 1003-1009.  
<https://doi.org/10.2514/3.5267>
- [9] Baresi, N., Dei Tos, D. A., Ikeda, H., and Kawakatsu, Y., "Trajectory Design and Maintenance of the Martian Moons eXploration Mission around Phobos," *Journal of Guidance, Control, and Dynamics*, Vol. 44, No. 5, 2021, pp. 996-1007.  
<https://doi.org/10.2514/1.G005041>
- [10] Bernardini, N., Baresi, N., and Armellin, R., "Fuel-Efficient Stationkeeping of Quasi-Satellite Orbits via Convex Optimization," *Journal of Guidance, Control, and Dynamics*, Vol. 46, No. 12, 2023, pp. 2421-2431.  
<https://doi.org/10.2514/1.G007557>
- [11] Chen, H., Canalias, E., Hestroffer, D., and Hou, X., "Effective Stability of Quasi-Satellite Orbits in the Spatial Problem for Phobos Exploration," *Journal of Guidance, Control, and Dynamics*, Vol. 43, No. 12, 2020, pp. 2309-2320.  
<https://doi.org/10.2514/1.G004911>
- [12] Hénon, M., "Numerical Exploration of the Restricted Problem, V. Hill's Case: Periodic Orbits and Their Stability," *Astronomy and Astrophysics*, Vol. 1, 1969, pp. 223-238.
- [13] Bezrouk C., and Parker J., "Long Duration Stability of Distant Retrograde Orbits," *AIAA/AAS Astrodynamics Specialist Conference*, AIAA, 2014, pp. 4424.  
<https://doi.org/10.2514/6.2014-4424>
- [14] Tan, M., Zhang K., and Wang J., "Strategies to Capture Asteroids to Distant Retrograde Orbits in the Sun-Earth System," *Acta Astronautica*, Vol. 189, 2021, pp. 181-195.  
<https://doi.org/10.1016/j.actaastro.2021.08.041>

- [15] Condon, G. L., and Williams J., "Asteroid Redirect Crewed Mission Nominal Design and Performance," *SpaceOps 2014 Conference*, 2014, pp. 1696.  
<https://doi.org/10.2514/6.2014-1696>
- [16] Conte, D., Di Carlo M., Ho K, Spencer D. B., and Vasile M., "Earth-Mars Transfers Through Moon Distant Retrograde Orbits," *Acta Astronautica*, Vol. 143, 2018, pp. 372-379.  
<https://doi.org/10.1016/j.actaastro.2017.12.007>
- [17] Pushparaj, N., Baresi, N., Ichinomiya, K., and Kawakatsu, Y., "Transfers around Phobos via Bifurcated Retrograde Orbits: Applications to Martian Moons eXploration Mission," *Acta Astronautica*, Vol. 181, 2021, pp. 70-80.  
<https://doi.org/10.1016/j.actaastro.2021.01.016>
- [18] Strange, N. J., Lam, T., Russell, R. P., and Spilker, T. R., "Study on the Stability of Science Orbits of Enceladus," *AAS/Division for Planetary Sciences Meeting Abstracts*, Vol. 38, 2006, pp. 24-09.
- [19] Koon, W. S., Lo, M. W., Marsden, J. E., and Ross, S. D., *Dynamical Systems, the Three-body Problem and Space Mission Design*, Marsden Books, 2011, pp. 174-175.
- [20] Szebehely, V., *Theory of Orbits: The Restricted Problem of Three Bodies*, Academic Press, 1967, pp. 16-21.
- [21] Oshima K., "Continuation and station keeping analyses on planar retrograde periodic orbits around the Earth," *Advances in Space Research*, Vol. 69, No. 5, 2022, pp. 2210-2222.  
<https://doi.org/10.1016/j.asr.2021.12.020>
- [22] Muralidharan, V., Weiss, A., and Kalabic, U. V., "Control Strategy for Long-Term Station-Keeping on Near-Rectilinear Halo Orbits," *AIAA Scitech 2020 Forum*, 2020, pp. 1459.  
<https://doi.org/10.2514/6.2020-1459>
- [23] Liang, Y., and Hyodo, R., "Giga-year Dynamical Evolution of Particles around Mars," *Icarus*, Vol. 391, 2023, pp. 115335.  
<https://doi.org/10.1016/j.icarus.2022.115335>
- [24] Douskos, C. N., and Markellos, V. V., "Out-of-plane Equilibrium Points in the Restricted Three-Body Problem with Oblateness," *Astronomy & Astrophysics*, Vol. 446, No. 1, 2006, pp. 357-360.  
<https://doi.org/10.1051/0004-6361:20053828>
- [25] Sharma, R. K., and Subba Rao, P. V., "Stationary Solutions and Their Characteristic Exponents in the Restricted Three-Body Problem When the More Massive Primary is an Oblate Spheroid," *Celestial mechanics*, Vol. 13, No. 2, 1976, pp. 137-149.  
<https://doi.org/10.1007/bf01232721>
- [26] Keller, H. B., "Numerical Solution of Bifurcation and Nonlinear Eigenvalue Problems," *Applications of Bifurcation Theory*, 1977.

- [27] Lara, M., Russell, R., and Villac, B., "Classification of the Distant Stability Regions at Europa," *Journal of Guidance, Control, and Dynamics*, Vol. 20, No. 2, 2007, pp. 409-418.  
<https://doi.org/10.2514/1.22372>
- [28] Doedel, E. J., Paffenroth, R. C., Keller, H. B., Dichmann, D. J., Galán-Vioque, J., and Vanderbauwhede, A., "Computation of Periodic Solutions of Conservative Systems with Application to the 3-Body Problem," *International Journal of Bifurcation and Chaos*, Vol. 13, No. 06, 2003, pp. 1353-1381.  
<https://doi.org/10.1142/S0218127403007291>
- [29] Peng, L., Liang, Y., Pushparaj, N., and Shi, P., "Quasi-solar Synchronous Orbit around the Moon based on Spatial Distant Retrograde Orbits," *74th International Astronautical Congress*, International Astronautical Federation Paper 77326, 2023.
- [30] Campbell, E. T., "Bifurcations from Families of Periodic Solutions in the Circular Restricted Problem with Application to Trajectory Design," Ph.D. Dissertation, Purdue Univ., 1999.
- [31] Liang, Y., Xu, M., Peng, K., and Xu, S., "A Cislunar in-orbit Infrastructure Based on  $p:q$  Resonant Cycloidal Orbits," *Acta Astronautica*, Vol. 170, 2020, pp. 539-551.  
<https://doi.org/10.1016/j.actaastro.2020.02.029>
- [32] Hubaux, C., Lemaitre, A., Delsate, N., and Carletti, T., "Symplectic Integration of Space Debris Motion Considering Several Earth's Shadowing Models," *Advances in Space Research*, Vol. 49, No. 10, 2012, pp. 1472-1486.  
<https://doi.org/10.1016/j.asr.2012.02.009>
- [33] Ye, B., Zhang, X., Ding, Y., and Meng, Y., "Eclipse Avoidance in TianQin Orbit Selection," *Physical Review D*, Vol. 103, No. 4, 2021, 042007.  
<https://doi.org/10.1103/PhysRevD.103.042007>
- [34] Macdonald, M., McKay, R., Vasile, M., and Frescheville, F. B. D., "Extension of the Sun-Synchronous Orbit," *Journal of Guidance, Control, and Dynamics*, Vol. 33, No. 6, 2010, pp. 1935-1940.  
<https://doi.org/10.2514/1.49011>
- [35] Gao, S., Zhou, W., Zhang, L., Liang, W., Liu, D., and Zhang, G., "Trajectory Design and Flight Results for Chang'e-4 Relay Satellite (in Chinese)," *Scientia Sinica Technologica*, Vol. 49, 2019, pp. 156-165.  
<https://doi.org/10.1360/N092018-00393>